https://doi.org/10.1038/s40494-026-02873-1

Mobile terahertz spectroscopy for in-situ evaluation of structural characteristics in wooden artefacts

Check for updates

Cornelius Mach[1], Roksana Jachim[2], Jan Ornik[1], Alexander Jäckel[1], Jochen Taiber[1], Enrique Castro-Camus[3], Rudy Plarre[4], Martin Koch[1], Wolfgang Viöl[2] & Kirsti Krügener[2] ✉

Conserving fragile wooden artworks requires diagnostics that detect minimal structural changes without invasive intervention. We used a robotic-arm terahertz time-domain spectroscopy (THz TDS) system to study the centrepiece of the Marienaltar in Isenhagen Monastery (Hankensbüttel, Germany), a polychrome, gilded winged altarpiece from the early 16th century. Analyses revealed severe limewood deterioration from insect damage (notably *Anobium punctatum*) and fungal activity linked to fluctuating climate; prior restorations were identified via archives, visual inspection, and material analysis. Due to the object's fragility, restoration was performed in situ. Robotic THz TDS enabled non-contact measurements before and after treatment, assessing sensitivity to subtle structural changes from consolidation. Results show THz TDS detects millimetre-scale changes beneath the polychromy, providing objective evidence of treatment effectiveness. This case demonstrates the potential of robotic THz TDS for long-term monitoring and quantifying restoration impact, advancing evidence-based conservation.

Wooden artworks represent a distinctive component of cultural heritage, characterised by their intended permanence and accessibility. However, this very quality renders them susceptible to degradation when exposed to environmental conditions. A wide range of factors can compromise the structural integrity and long-term preservation of cultural heritage sites. These include climatic fluctuations, chemical reactions, biological activity and enzymatic processes as well as anthropogenic deterioration caused by reasons that range from neglect to invasive restoration techniques[1–5]. In order to ensure their survival, it is necessary to implement monitoring strategies that mitigate risks while also ensuring the safeguarding of both their aesthetic and historical value.

In recent decades, a wide range of scientific examination methods have been incorporated to the field of restoration science allowing to assess the condition of historic wood with increasing precision. In the context of architectural heritage conservation, non-destructive testing (NDT) methods such as X-ray imaging, ultrasonic testing and percussive testing are commonly applied to investigate wooden structures, as well as methods like ground-penetrating radar (GPR) and magnetic resonance imaging (MRI) have been explored primarily in research contexts[6–8]. However, when it comes to the conservation of wooden sculptures and artworks, many of these methods are not routinely applied due to the limited equipment portability, object size constraints, radiation safety regulations and the need for high spatial resolution. For example, GPR and MRI are not widely used, as their applicability is limited to specific structural contexts and their operational requirements often exceed what is feasible for routine restoration practice. These requirements include not only logistical constraints such as limited portability and object-size restrictions, but also the need for specialised facilities, long acquisition times, and in the case of MRI strict safety and shielding conditions, which make routine in-situ use impractical. In selected cases, X-rays or computed tomography (CT), resonance-acoustic sensors for percussion testing or ultrasonic testing have been employed to assess structural features and material integrity in wooden artefacts. Although these methods can reveal internal features and hidden damage, each technique has specific limitations. Radiography, for example, provides only two-dimensional projections, while CT requires exposure to large doses of ionising radiation, thus requiring specialised facilities, and ultrasound or acoustic techniques are constrained by limited depth resolution and sensitivity. Their overall applicability is further restricted by physical contact requirements, lack of *in-situ* applicability, and high operational costs. Moreover, the moisture content of wood—an essential parameter influencing mechanical and acoustic behaviour—can significantly affect

[1]Department of Physics and Material Sciences Center, Philipps-Universität Marburg, Marburg, Germany. [2]Faculty of Engineering and Health, HAWK University of Applied Sciences and Arts, Göttingen, Germany. [3]Centro de Investigaciones en Optica A.C., Lomas del Campestre, Leon, Mexico. [4]Federal Institute for Materials Research and Testing, Berlin, Germany. ✉e-mail: kirsti.kruegener@hawk.de

the measurement accuracy but is often insufficiently controlled during the examination procedures[9–11].

In practical conservation, wooden objects are usually treated on-site, and sampling is often not possible. Consequently, wood evaluation is largely limited to archival research, visual inspection, and dendrochronology. Assessments primarily rely on visible damage patterns, while deep structural deterioration is typically only estimated 'by experience'. Furthermore, the correlation between visible deterioration and internal structural condition of wood is often weak, making visual assessment insufficient for reliable diagnostics.

In many cases, even severely damaged wooden objects are transported or moved before a comprehensive structural assessment has been carried out, which may increase the risk of secondary fractures and losses during the handling and conservation[12–14]. The experience-based approach can lead to inconsistent and limited diagnostic reliability. This may result in unsuitable transportation or handling strategies, and in the precautionary application of consolidation agents or environmentally hazardous biocides. Such practices not only jeopardise the integrity of the artefacts but also pose risks to conservators and handlers.

Therefore, the structural analysis of fragile wooden artworks remains challenging, particularly owing to the limited availability of widely applicable diagnostic methods that meet modern conservation standards. Current conservation practice increasingly demands contact-free, non-invasive techniques that preserve the material integrity and are ideally applicable in situ, in accordance with established conservation ethics and guidelines[15,16]. The ability to clearly distinguish between intact, consolidated and deteriorated wood would allow the frequency and scope of consolidation and biocide treatments to be adapted to the actual conservation requirements of each piece. To date, this kind of concretisation remains a research *desideratum* in conservation science. The goal is to reliably assess the structural integrity of an object prior to an intervention. This knowledge is fundamental for planning safe-handling, transportation, and conservation procedures, and enables stakeholders—including museums, churches, monasteries, and private collectors—to make safe decisions regarding the loan, storage, and exhibition of wooden artefacts.

Terahertz (THz) analysis of culturally valuable artefacts is an emerging field, which allows contact-free, non-ionising and harmless subsurface inspection[17]. Recent advancements, like fibre-coupled THz antennas, miniaturisation of lasers and the development of compact off-the-shelf measurement systems[18] make measurements of cultural objects more feasible than it was a couple of decades ago. These developments allowed the integration of a THz measurement head with a robotic arm like the system used in this paper. This setup was first demonstrated 2017[19] and makes it possible to examine objects with complex three-dimensional shapes. For example, it was shown that damage on wood caused by insects can be detected[20]. Furthermore, an almost 3000-year-old mummified Egyptian hand was also examined[21] successfully reconstructing various layers in it.

Recent studies of cultural objects with THz spectroscopy include the inspection of archaeological and historical ceramics with[22,23] and without glazing[24,25] as well as the examination of damages in stone relics and sculptures[26,27]. Other applications of THz spectroscopy include the analysis of composition and structure of the different layers in paintings and coloured panels[28–30], as well as the discernment of letters in damaged historical scriptures[31] or the revelation of inscriptions on a weathered leaden cross[32]. This large diversity of applications of the THz technology on cultural artefacts is further bolstered by ref. 33 and shows its great potential within this field.

Methods

Terahertz time-domain-spectroscopy

Terahertz waves, just like visible light, are a type of electromagnetic radiation. It turns out that the majority of pigments, adhesives and other non-metallic materials used in cultural heritage manufacture and conservation are, at least partly, transparent to terahertz waves[34]. This opens the possibility to examine the structure of those objects with THz systems, thus finding interfaces between materials, voids, cracks and other internal features. The measurements in this paper were performed using Terahertz Time-Domain-Spectroscopy (THz-TDS). In simple terms, this means that THz pulses, which have very short temporal duration, are used to illuminate the sample. As these very short pulses propagate through the sample they encounter interfaces, voids, cracks, etc. and each one of them produces a reflected 'echo' which propagates in the backwards direction as depicted in Fig. 1a). Those reflected pulses are then recorded by the detector as a function of time. Therefore, by knowing the temporal separation between these echoes it is possible to infer the position and shape of the interface that produced them, when the dielectric properties (e.g. refractive index) of the investigated materials are known or can be estimated, thereby providing us with a tool to map the three-dimensional internal structure of the object. This particular measurement scheme is called THz tomography[35,36].

THz-TDS[37,38] itself is a relatively new technique and its use in the field of cultural heritage is still seeing its early development. We will not discuss the details of measurement scheme here, instead the interested reader is referred to ref. 37 for details. THz TDS was initially driven mainly by the field of materials science[39–46], yet it quickly evolved into an imaging technique[36,47–50] applicable to NDT in a variety of scenarios. Just under 20 years ago, a new antenna material was introduced that also allowed fibre lasers to be used as excitation sources[51]. This enabled the development of fibre-coupled THz spectrometers, which offer a much higher degree of flexibility and stability[52,53].

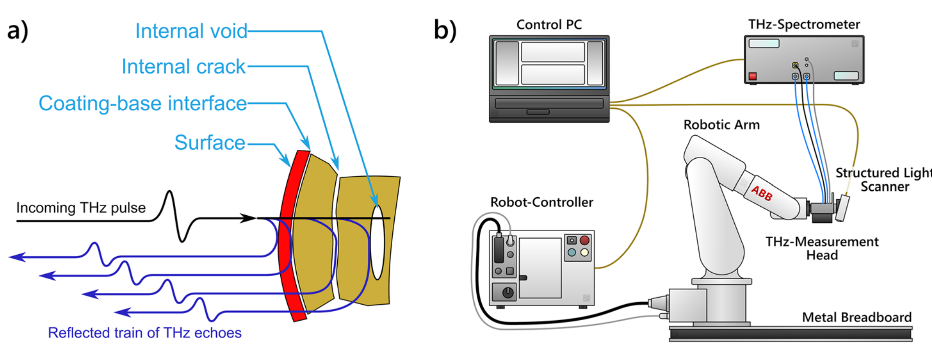

Fig. 1 | Schematic overview of THz pulse interaction with internal structures and the robotic-arm-based measurement setup. Schematic representation of reflected echoes from internal structure of an object under study (**a**) and schematic setup of the robotic-arm-based THz measurement system (**b**). **a** Demonstrates schematically, how an incoming THz pulse gets reflected in a train of echoes by different internal features of an object under study. The object is presented here as a bisection with the surface layer shown in red, the bulk material in dark yellow and internal features in white. **b** Shows schematically, how the different parts of the robotic-arm-based THz measurement system are set up, attached and connected by cables. Here blue lines correspond to glass fibres, yellow lines to data cables, while black and grey lines correspond to supply and readout cables.

THz material properties

Prior to the in-situ object measurements, extensive laboratory characterisation was carried out to establish a reliable basis for interpreting the THz data. This included systematic transmission and reflection THz-TDS measurements on reference specimens of (*Tilia sp.*) with controlled insect infestation by *Anobium punctatum*, and on a range of materials commonly used in historical and contemporary conservation practices, as well as in the one we performed. The presence of *Anobium punctatum* infestation on the altar was established by the recovery of beetle specimens and by characteristic signs of wood damage (frass, exit holes and galleries) observed on the object. Collected specimens were identified morphologically by comparison with the taxonomic literature and by confirmation at an external taxonomic reference laboratory. Suspected microbial colonisation was verified by targeted sampling and cultivation at the microbiology laboratory of HAWK, where isolates were examined and identified using routine culture-based methods. Controlled *Tilia* sp. specimens with known *A. punctatum* infestation were used in the laboratory THz-TDS characterisation to provide reference spectra for interpreting the in-situ measurements. It is imperative to identify these materials prior to conducting practical measurements. In the course of this research project, THz-TDS was utilised for the characterisation of all materials examined, including, filling materials and consolidants. It is posited that these findings may be extrapolated to future studies of wooden artefacts. The dielectric parameters, i.e. the refractive index and the absorption coefficient of the materials under analysis acquired through THz transmission measurements, are shown in Fig. 2. The goal was to determine the refractive index and absorption coefficient across the THz band, thereby enabling a material-specific interpretation of reflection-mode measurements.

For the transmission measurements samples with flat and parallel surfaces and thicknesses ranging from 1.0 to 5.5 mm were prepared as follows: The champagne chalk-based putties as well as the phenolic resin-based filler were each cast into a plastic frame in which they solidified as cuboids. Sturgeon glue and Degalan® P28 were ground into fine powder and compressed into cylindric tablets, while for the lime wood clusters a total of eleven equally cut, flat pieces of lime wood with differing year ring orientations were prepared. All samples were measured under Nitrogen atmosphere in a focused THz TDS transmission setup using the same TeraWave THz spectrometer employed later for the robotic arm-based THz measurements. The larger lime wood samples were measured at 81 positions in a 9×9 grid while the other samples were measured at 9 positions in a 3×3 grid to account for possible inhomogeneities. These latter measurements were repeated thrice for statistics and for each sample several reference measurements were taken. The thickness of each sample was measured with a micrometre screw gauge and all samples were evaluated with the software TeraLyzer from MenloSystems GmbH. For the lime wood samples two clusters with very similar results emerged. These results were compiled into the two presented clusters consisting of the averaged results of seven (cluster 1) and of four (cluster 2) lime wood pieces.

The error bars visible in Fig. 2 are determined from error propagation of the statistical error together with the background noise floor and an assumed deviation of 2 μm from the acquired thickness.

The refractive index and absorption coefficient values across the THz band of the tested materials are summarised in Table 1.

These values show several important trends. Materials with refractive indices close to that of Lime wood (Tilia sp.) ($n = 1.24–1.36$), such as Degalan® P28 ($n = 1.41$) and the phenolic resin mixture ($n = 1.14$), are likely to produce weak or indistinct reflections in THz imaging, making them difficult to differentiate from the original substrate. In contrast, materials with significantly higher refractive indices, such as Champagne Chalk in hide glue ($n = 2.16$) or isinglass ($n = 1.79$), are expected to generate more pronounced reflection signals at material interfaces. However, these same materials also exhibit higher absorption coefficients, which can lead to strong attenuation or even complete loss of the THz signal, especially at higher frequencies.

This frequency-dependent transparency is particularly relevant for practical applications. Most of the composite materials tested showed reliable signal transmission only at lower frequencies (below ~1 THz). Yet, Degalan®, the phenolic resin mixture and Champagne Chalk in 8% hide glue show a good transparency also at higher frequencies. This limits the usable spectral range for in-situ diagnostics and necessitates careful selection of frequency bands when targeting specific materials or interfaces. For instance, while high-index fillers may be clearly visible at low frequencies, their strong absorption can obscure deeper layers or underlying structures, especially in multi-layered or restored regions.

These findings underscore the critical importance of prior material characterisation. Without precise knowledge of the dielectric properties of conservation materials, the interpretation of THz reflection data remains ambiguous. By integrating laboratory-derived reference values into the analysis workflow, it becomes possible to distinguish between original wood, conservation compounds, and potential voids or damage zones with greater confidence. This enhances the diagnostic value of THz imaging and

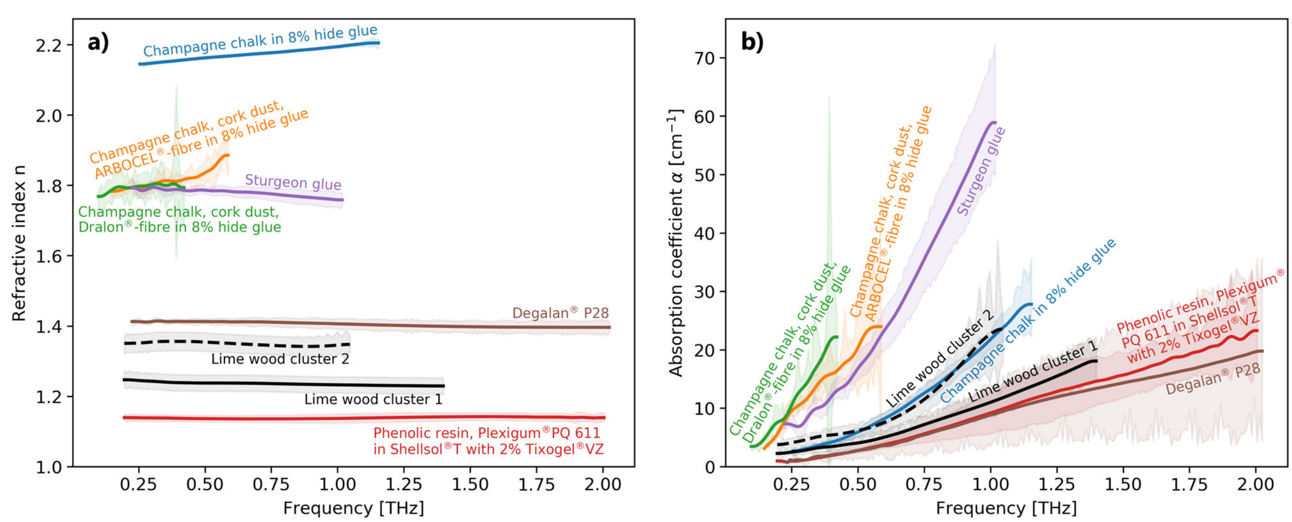

Fig. 2 | Frequency-dependent refractive index and absorption coefficient of lime wood and conservation materials measured by THz-TDS. THz refractive index (**a**) and absorption coefficient (**b**) of materials used during restoration and of lime wood samples grouped into two clusters as comparison. **a** Shows the frequency-dependent refractive index acquired from THz transmission measurements. **b** Shows the frequency-dependent absorption coefficient in inverse centimetres acquired from the same THz transmission measurements. Each curve is labelled with its corresponding material in the same colour in both panels and the shaded areas surrounding the curves indicate the measurement uncertainty.

Table 1 | THz properties of relevant materials at selected frequencies

No.	Material and material composition	Refractive index (n)		Absorption coefficient (α) [1/cm]	
		@ 0.4 THz	@ 1.0 THz	@ 0.4 THz	@ 1.0 THz
1	Champagne Chalk in 8% hide glue	$2.16^{+0.00}_{-0.01}$	$2.19^{+0.01}_{-0.00}$	$4.2^{+0.3}_{-0.6}$	$21.7^{+1.4}_{-1.6}$
2	Champagne Chalk, cork dust, ARBOCEL® (powdered cellulose) in 8% hide glue	$1.81^{+0.02}_{-0.02}$	-	$15.9^{+3.4}_{-3.2}$	-
3	Champagne Chalk, cork dust, Dralon® staple fibres, 4 mm in 8% hide glue	$1.80^{+0.08}_{-0.04}$	-	$21.9^{+12.1}_{-12.7}$	-
4	Sturgeon bladder glue (isinglass)	$1.79^{+0.01}_{-0.01}$	$1.76^{+0.02}_{-0.02}$	$12.1^{+2.0}_{-1.3}$	$58.5^{+11.3}_{-10.6}$
5	Degalan® P28	$1.41^{+0.01}_{-0.01}$	$1.41^{+0.01}_{-0.01}$	$2.0^{+1.0}_{-0.8}$	$8.8^{+5.5}_{-5.4}$
6a	Lime wood (Tilia sp.), cluster 1	$1.24^{+0.02}_{-0.02}$	$1.23^{+0.02}_{-0.02}$	$3.5^{+1.0}_{-0.9}$	$11.0^{+2.1}_{-2.2}$
6b	Lime wood (Tilia sp.), cluster 2	$1.36^{+0.03}_{-0.03}$	$1.35^{+0.04}_{-0.03}$	$5.4^{+1.3}_{-1.1}$	$22.6^{+10.9}_{-8.2}$
7	Organic phenolic resin hollow spheres, Plexigum® PQ 611 in Shellsol® T with 2% Tixogel® VZ.	$1.14^{+0.01}_{-0.01}$	$1.14^{+0.01}_{-0.01}$	$1.9^{+0.2}_{-0.3}$	$9.2^{+3.6}_{-3.6}$

supports more informed conservation decisions, particularly in cases where sampling is not feasible and non-invasive methods are essential.

Measurement setup

The measurements were performed using the THz measurement system schematically shown in Fig. 1b). The main pieces of this system are an IRB-120 robotic arm from ABB with an attached THz measurement head as well as a David3D structured light scanner and a TeraWave THz-TDS spectrometer from Fraunhofer HHI. The THz measurement head consists of a modified THz reflection head from Fraunhofer HHI, where possible collision sources were removed and the casing was strengthened for additional attachments to the robotic arm. It contains two fibre-coupled photoconductive THz antennas, one emitter and one detector, as well as four 90° off-axis parabolic mirrors (OAPM) with 1-in. diameter. The generated THz radiation is first collimated by an OAPM with 2-in. focal length. The collimated beam is then focused by an OAPM with a 4-in. focal length into the focal plane around 10 cm away from the measurement head. The beam is incident on the sample at an angle of 8° and has a focus diameter of approximately 1 mm at 1 THz. The reflected beam is collected and collimated by a second OAPM with 4-in. focal length and the last OAPM with 2-in. focal length focuses the THz radiation onto the detector antenna. Both antennas are connected via optical fibres to the laser incorporated in the THz spectrometer and with coaxial cables to the bias voltage source and THz signal acquisition electronics. The THz measurement head includes a structured light scanner, consisting of a projector and a camera. The structured light scanner allows measuring the 3-dimensional surface of the object in order to guide the motion of the robotic arm. The robotic arm is mounted on a heavy metal breadboard, which provides a stable base and acts as an inertia damper for the robotic arm. The movements of the robotic arm itself are powered and controlled by an IRC5 robot-controller from ABB. The robot-controller, THz spectrometer and structured light scanner are attached to a control and measurement computer, which coordinates measurements and movements and acquires the measured data.

Measurement process

We performed two measurement campaigns to acquire the THz data, which are presented here. The first measurement campaign was performed before the restoration and the second one was carried out around half a year later, after the restoration work had been completed. For each campaign, the THz measurement setup described above was assembled and calibrated following the same procedure to ensure comparability of the datasets.

This calibration procedure is a longer process that relates the coordinate systems of the robotic arm, THz-measurement head and the 3D-scanner and ensures correct positioning of the THz-measurement head with respect to the object scanned with the 3D-scanner. This is primarily done via a reference pattern that is fixed to the same breadboard as the robotic arm. After internally calibrating the robotic arm servo motors through alignment of reference notches in its casing, the position and orientation of the reference pattern is determined in robotic arm coordinates through physical contact and alignment of a metal thorn attached to the robotic arm. Afterwards the thorn is removed and the THz measurement head together with the structured light scanner are attached to the robotic arm. Subsequently, the position and angle of the structured light scanner is calibrated to the reference pattern through a projected positioning grid. After this the 3D-scanner is calibrated by scanning a separate calibration plate dedicated to this task. With the calibrated 3D-scanner the original reference pattern is scanned and the remaining calibration parameters of the structured light scanner are calculated from the position of the scanned pattern. With this the coordinate systems of the 3D-scanner and the robotic arm are directly related. The next step is to calibrate the THz measurement head to these unified coordinate systems, by first determining the correct positioning angle and then acquiring the correct distance through consecutive measurements on a flat reference metal surface. After this, the lateral position of the THz measurement head is calibrated through measurements over a metal edge placed along to the already calibrated projection grid. When this is done, all coordinate systems are related and a verification measurement on a metal reference is performed. If the result is satisfactory, the integrated THz-robotic-arm-system is deemed calibrated. If not, the necessary calibration steps are repeated.

After the calibration, the breadboard with the robotic arm and measurement setup was placed in front of the sculpture of Mary with the infant Jesus, which was temporarily removed from the altar during the examination and restoration period. Prior to the THz acquisition the sculpture was fully scanned in several steps with the structured light scanner. These scans were then combined into a 3D model of the whole sculpture, which is used in a simulation at a later step in order to control the motion of the robotic arm during the point-by-point acquisition of the terahertz reflection waveforms. Figure 3 shows photos of the measuring campaign.

Two measurement areas on the sculpture were chosen, one located on the knee of Mary and the other on the hips of the infant Jesus. These regions were selected given that restoration treatments were planned and performed in these areas as well as due to their accessibility with the robotic-arm-based THz measurement system. The entire Marienaltar, including the figures surveyed using THz-TDS, was treated as part of a single restoration campaign; interventions were carried out on a case-by-case basis depending on the condition of the object and its requirement. Therefore, no quantitative, percentage-based map of treatment intensity is available for the entire object. In addition, several conservation measures, particularly consolidation treatments and the re-adhesion of lifting polychromy, affect subsurface structures beyond the visibly treated areas, making a purely surface-based mapping only partially representative of the actual material changes detectable with THz TDS. The two THz measurement areas were selected because they were accessible and had undergone consolidation and filling following preliminary examinations;

Fig. 3 | Photographs of measurements with the robotic arm on the sculpture of Mary with infant Jesus. a Shows the 3-dimensional mapping process of an area with the structured light scanner. **b** Shows the THz measurement at the same measurement area with the structured light scanner removed.

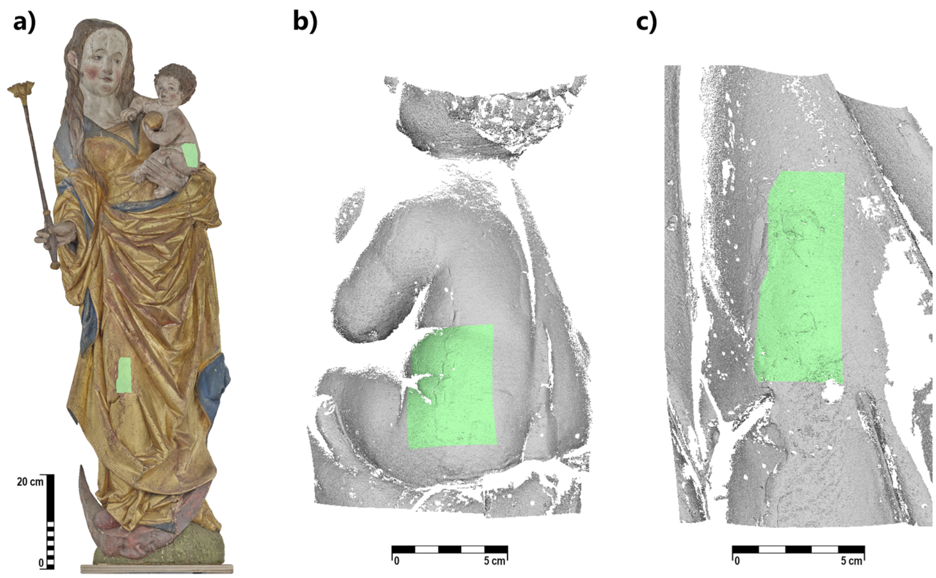

Fig. 4 | Photogrammetric reference image and structured-light 3D scans of the Marienskulptur with digitally marked THz measurement areas. Photogrammetric image (**a**) and 3D scans (**b**, **c**) of the sculpture of Mary with infant Jesus with the measurement areas digitally marked in green and with added scalebars. **a** Shows the frontal orthogonal projection of a photogrammetric image for the whole sculpture provided by fokus GmbH Leipzig. **b**, **c** show the surface mesh of the 3D scan acquired with the structured light scanner with (**b**) displaying the 3D scan image of the infant Jesus and (**c**) the 3D scan image of the knee of the Virgin Mary sculpture.

they thus serve as representative test areas for recording pre- and post-restoration changes with THz-TDS. Both regions are marked in green in the photogrammetric image of the sculpture in Fig. 4a), provided by fokus GmbH Leipzig. For each of the measurement areas, a higher resolution scan was performed using a structured light scanner to obtain more detailed surface information. Figure 4b, c) illustrate the resulting 3D models. Once again, the areas where THz measurements were taken are digitally marked in green.

The 3D models which were obtained using the structured light scanner and which are shown in Fig. 4b, c are used to create a THz measurement path. In order to achieve this objective, a 1 by 1-mm grid of the desired size was projected onto the 3D model. Thereafter, the surface normal at each grid point was calculated. Subsequently, position and orientation of the robotic arm in relation to each measurement point are calculated in such a manner that the THz measurement head is always positioned at the appropriate distance from the surface of the sculpture. Furthermore, the THz measuring head is oriented such that its main axis is always perpendicular to the surface section to be examined. The movement pattern of the robotic arm that resulted from this process was then simulated in the software programme RobotStudio®. In the course of this simulation, measurement points that are unreachable are eliminated. Besides, movements that would result in collisions of the measurement head with the sculpture, are eliminated. Subsequently, the terahertz measurement can be conducted in a safe manner. Figure 3b) shows a photo taken during the THz measurement process on the hip of the infant Jesus. The structured light scanner was detached from the measurement head during the THz measurements. This precautionary measure was implemented to ensure enhanced safety and stability during the robotic arm movement.

In addition to the THz measurements of the areas of interest on the sculpture, reference and background measurements were carried out with the robotic-arm-based THz system. The air background THz measurements were performed on empty space with a distance of at least 35 cm between the measurement head and any surface to exclude possible reflections. The reference measurements were all performed on the same flat metal surface, with the THz measurement head positioned at the known optimal distance. These reference measurements are necessary for data evaluation and to assess system stability and make the data comparable between measurements.

Restoration

Initial Condition: The sculpture showed indications of local material losses, areas of structural collapse, and subsurface zones of reduced cohesion attributable to infestation by common furniture beetle (*Anobium punctatum*). Furthermore, the presence of mould was observed in various locations. The polychrome layers exhibited indications of partial detachment and losses. Previous restorative procedures were discernible. In certain areas, a combination of defined and undefined materials, including biocides

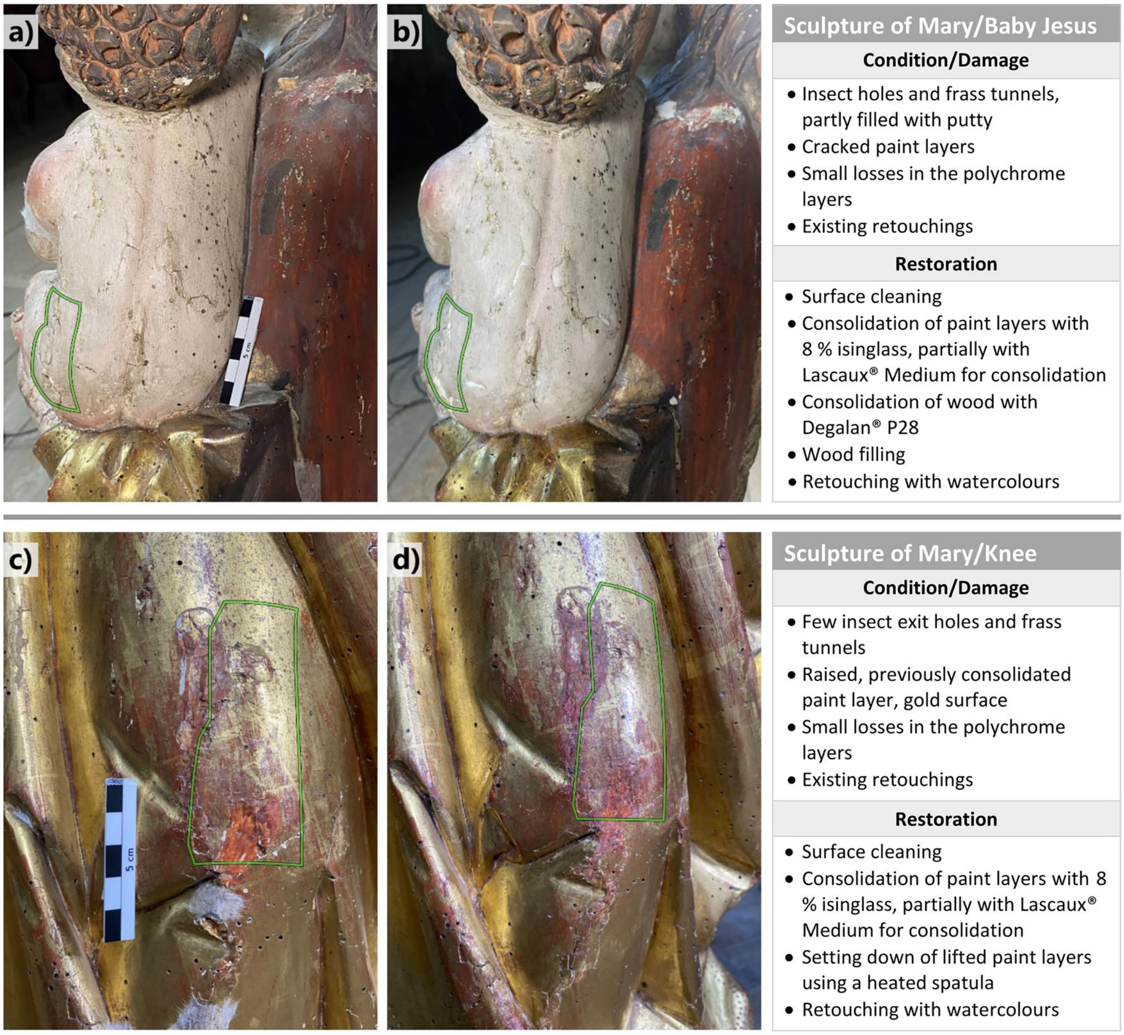

Fig. 5 | Photographs of the measurement areas before, during and after restoration with marked THz measurement areas. The measurement areas are digitally marked in green and with description of the corresponding condition before restoration and the performed restorative measures on the right. The upper row relates to the infant Jesus section of the virgin Mary sculpture with photographs before restoration (**a**) and during restoration (**b**). The lower row relates to the knee of the Virgin Mary sculpture with photographs before (**c**) and after restoration measures (**d**).

and consolidants, had already been utilised. Consequently, in some areas newly applied consolidants were likely to be unable to penetrate sufficiently or establish effective adhesion, owing to pore blockage and limited interfacial compatibility with pre-existing saturated areas. As illustrated in Fig. 5, the condition of the sculpture's surfaces was meticulously examined prior to and following the restoration process, with particular attention to the designated measurement areas. The following measures were implemented as part of the restoration process:

Cleaning: Initially, the surface was meticulously brushed with soft-bristled brushes. Subsequently, an aqueous cleaning process was conducted, employing sponges to remove residual substances, followed by the superficial utilisation of solvents to ensure complete removal of these residues.

Wood Consolidation: In order to enhance the flow properties of the consolidant, initially a 5% solution of Degalan® P 28 in xylene/petroleum benzine (100–140 °C) was applied. Structural consolidation was then carried out by injecting a 25% solution Degalan® P 28 in xylene/petroleum benzine (100–140 °C). The consolidants for the wood were injected over cracks, losses and insect galleries using syringes until the material was saturated, in accordance with established conservation practice.

Wood Filling: Deep structural losses were filled with an injectable filler composed of phenolic resin hollow beads (0.005–0.127 mm) in Plexigum® PQ 611 with a slight addition of Tixogel®VZ. After sufficient drying, surface losses in the wood below the paint layer level were repaired using a solid wood filler consisting of cork flour, ARBOCEL® (powdered cellulose) in 8% hide glue, and chalk in hide glue.

Polychrome Layer Consolidation: The paint layer was consolidated using isinglass glue. However, in areas affected by previous restoration campaigns, adequate bonding could not be achieved. In these cases, Lascaux® Medium for consolidation was applied to provide additional stabilisation. Where necessary detached paint flakes were laid down using a heated spatula.

Polychrome Layer Filling: Losses in the polychrome layers were filled with a putty composed of Champagne Chalk in hide glue. It is plausible that some of the putty penetrated deeper into the wood substrate. Following drying, the surface of the filled areas was wet sanded, followed by the application of a thin shellac sealant in ethanol to prepare it for subsequent reintegration.

Retouching: The retouching process involved the application of watercolour paints for the purpose of chromatic reintegration. Gloss adjustment was achieved by varnish retouching with a solution of dammar resin in balsam turpentine oil.

The ultimate condition is as follows: The surface now appears superficially integrated and stabilised. Damaged areas in both the wood and the polychrome layers have been secured and filled in. However, the adhesion and depth of the fillings remain unclear in some cases. It is conceivable that

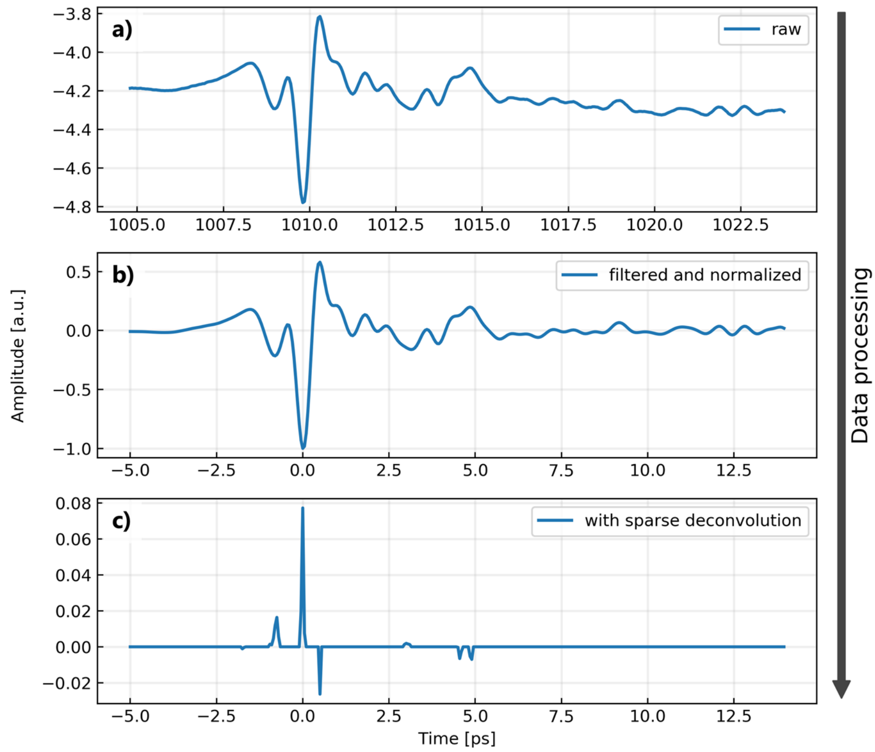

Fig. 6 | Example of the processing of a THz signal from one measurement point of the sculpture. **a** Shows the raw THz data before processing, **b** the amplitude data after normalisation and filtering with zeroing of the peak time-position and (**c**) shows the data further processed with sparse deconvolution algorithm making reflections easily discernible. All panels show the respective amplitude in arbitrary units dependent on measurement time in picoseconds.

previously consolidated historical areas may shift or detach due to the solvent set and the application of pressure, potentially resulting in local displacement or renewed detachment and subsequent internal losses.

Data processing

In order to be able to observe the changes produced by the restoration campaign, the terahertz data sets that correspond to the pre-restoration and post-restoration scans were matched using the software FreeCAD by using the previously acquired 3D-model of the object. The processing of the THz waveforms reflected by a single point of the sculpture is shown exemplarily in Fig. 6. Each panel shows the results of the sequential processing steps. The raw THz data can be seen in panel a) where a prominent pulse can be seen at about 1010 ps, this pulse is the reflection pulse from the surface of the sculpture. Another smaller pulse can be close to 1015 ps. This is a reflection pulse from an interface below the surface. These reflections below the surface are of interest to determine changes introduced by the restoration. In order to better evaluate the reflections, the THz data was filtered with a Butterworth bandpass filter in the range from 0.1 to 2.25 THz to remove noise. This filtering also removes any offset, so that the signal baseline becomes zero as shown in panel b). Afterwards the amplitude is normalised and the peak maximum is shifted to $t = 0$ ps. This assures that all surface peaks occur at the same time and removes the effects of the surface curvature. In order to better identify the reflections a sparse deconvolution algorithm was applied to the filtered and normalised THz data, for further details on this processing see[54–56]. The result of applying sparse deconvolution to the THz data from panel b) is shown in panel c). Since deconvolution moves the absolute time position, the data is shifted once again after the application of the algorithm so that the biggest peak of the surface is at the time position of 0 ps. In this panel it is much easier to discern the different layers of the sculpture at this measurement point from the different reflection peaks. The peaks described at the beginning in panel a) can be seen here much clearer and it can also be seen that the latter reflection peak coming a bit less than 5 ps after the surface peak actually corresponds to two peaks arising from two layers which are close together.

Figure 7 provides an illustration of the amalgamation of the fully processed results from both THz measurement campaigns for a specific measurement point on the sculpture. Arrows on the figure help the reader to identify layers close to the surface and deeper into the wood, which will be employed in the subsequent result section to elucidate the terminology. The THz results following sparse deconvolution are displayed in blue for the measurement prior to restoration, while the results for the measurement following restoration are shown in orange. The surface peaks, as previously described, are labelled and can be observed at a time position of 0 ps for both measurements. The region demarcated by a purple arrow and designated as 'surface layers' is situated between 0 and 3 ps. The term derives its nomenclature from the fact that reflection peaks within this range are generally directly associated with the surface and coating materials, which typically include the paint layers that may be present. The region adjacent to it is denoted by a black arrow and the annotation 'deeper reflections', which delineates the emergence of reflection peaks emerging from deeper non-surface layers, commencing at 3 ps and subsequently. This range is the primary focus when analysing the THz data. It is possible to see fluctuations in the time differences between peaks generated by the surface followed by peaks from subsurface layers. The appearance and disappearance of reflection peaks is related to changes occurring beneath the surface during the restoration process. As illustrated in the example data presented in the figure, following restoration, the deeper reflection peaks are observed to be delayed by approximately 0.25 ps. Concurrently, an additional stronger reflection peak emerges at the surface. The signals suggest that during the restoration process, an additional layer was applied to the surface of the sculpture at this specific point. The THz beam reflects from this new surface, and the thickness of the transmitted part and, consequently, the reflection from deeper layers are delayed.

As part of the analysis of the THz data, the effect of moisture content in the wood was taken into account. High moisture increases the THz absorption and reduce the penetration depth, which may prevent the evaluation of deeper reflections in some areas. This, however, is a consequence of the conditions of THz measurements on the 'real-world' objects. Therefore, during the *in-situ* measurements, it became clear that reliable values for the moisture content of the wood at depth could not be obtained, because THz waves cannot propagate deep enough.

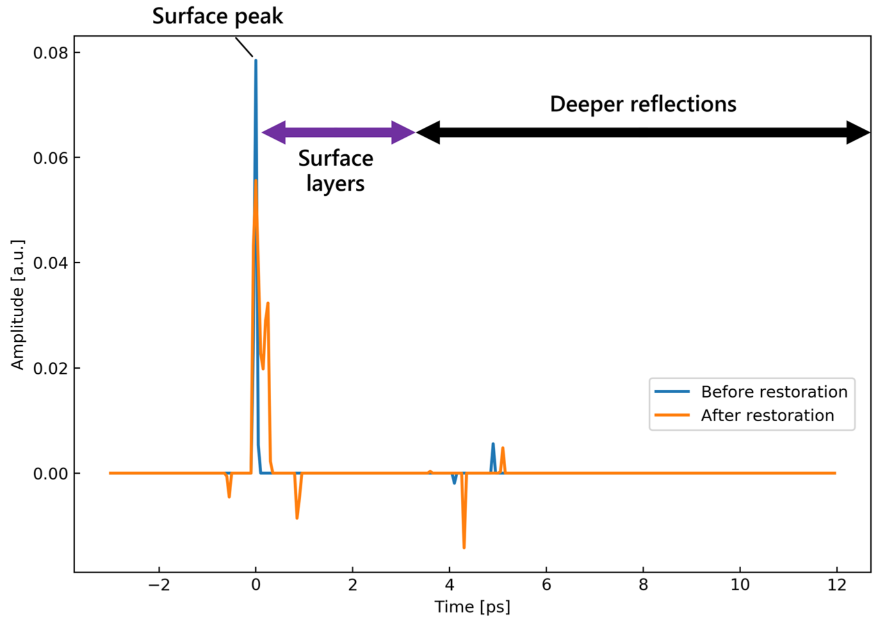

Fig. 7 | Fully processed THz time domain signals before and after restoration with annotated terminology. Fully processed THz time domain signals of the selected measurement point before restoration (blue curve) and after restoration (orange curve). The annotated surface peak marks the initial refl ection at the sculpture's surface. The region labelled surface layers (purple double headed arrow) highlights refl ections originating from near surface structures, while the region marked deeper refl ections (black double headed arrow) indicates refl ections from deeper internal interfaces.

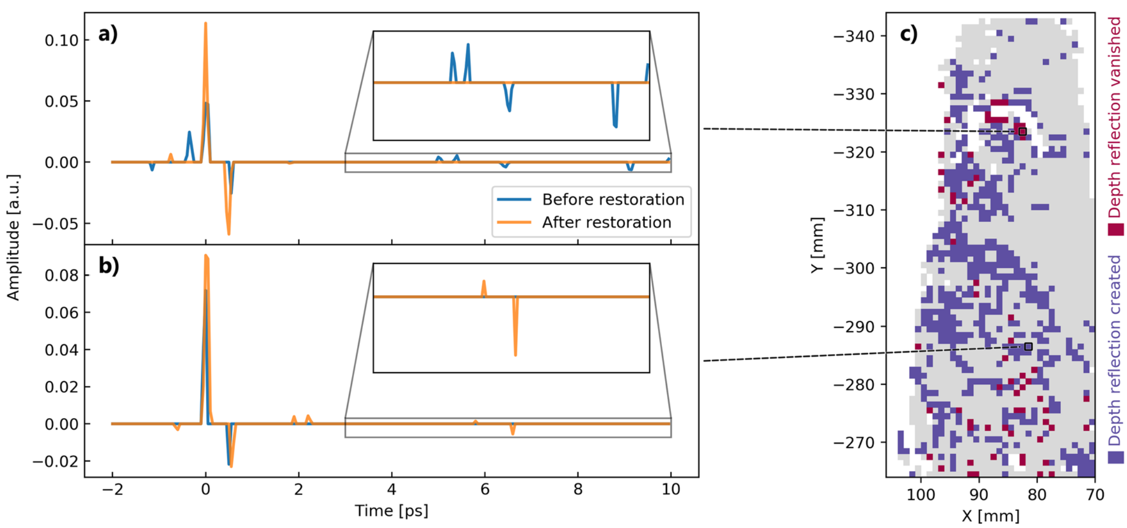

Fig. 8 | Introduction to the first THz data presentation scheme exemplarily shown for the measurement area on the knee of the sculpture of Mary. The colormap in (**c**) displays the first presentation scheme showing the spatial occurrence of reflections from subsurface layers that vanished (red) or were created due to restoration (blue), while grey points indicate positions where neither happened or the signal quality was too poor. The connection with the processed THz data is shown for particular positions in (**a**) for vanishing and in (**b**) for creation of deeper reflections. The enlarged sections highlight these changes.

Results

THz data presentation schemes

Many changes introduced during conservation are already visible on the surface, yet, the THz data gives us additional information with particular emphasis on alterations beneath the superficial layers. Two primary presentation schemes for the THz data will be used. These presentation schemes are introduced and explained first in the Figs. 8 and 9, while the comparison and interpretation of the results with regard to the corresponding restoration measures is shown afterwards in Figs. 10 and 11.

The first presentation scheme shown is the colormap displayed in Fig. 8c), which is presented exemplarily for the measurement area on the knee of the sculpture of Mary. The colormap illustrates the locations where deeper reflections in the THz data and, consequently, the corresponding subsurface layers have emerged (blue) or vanished (red) following the restoration process. Grey points indicate either that subsurface reflections neither vanished nor emerged or that the signal quality is insufficient for reliable evaluation. Panels (a) and (b) in the figure provide an illustrative representation of the relationship between the presentation scheme outlined in panel (c) and the processed THz measurement data. The two panels demonstrate the resulting THz amplitude of the measurements prior to and following restoration, in relation to the measurement time for the corresponding marked point in the colormap. In panel (a), which resembles a red point in the colormap, an enlarged section on the right reveals that deeper reflection peaks existed in the blue graph prior to restoration, but have since vanished in the orange graph following restoration. In a similar manner, in panel (b), which is denoted as a blue point in the colormap, it is possible to observe in the enlarged section that following restoration, deeper reflection peaks emerge in the orange graph. These were not present in the blue graph prior to restoration. In panel (c), clusters of disappearing and emerging

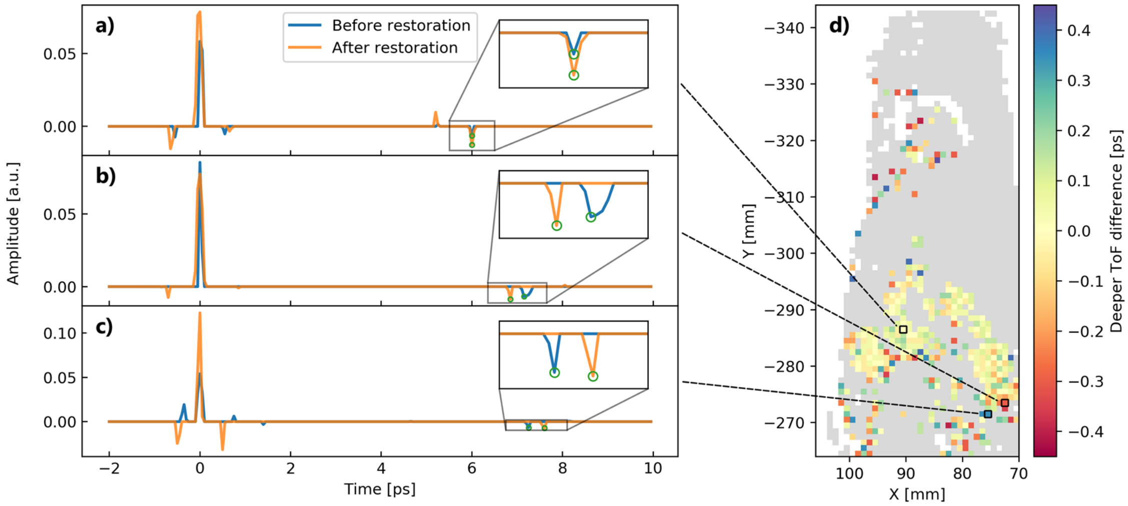

Fig. 9 | Introduction to the second THz presentation scheme exemplarily shown for the measurement area on the knee of the sculpture of Mary. The colormap in **d**) displays the second presentation scheme showing the spatial distribution of the time-of-flight (ToF) differences between deeper reflection pulses before and after restoration discernible through the colouring displayed in the colour bar, with grey points indicating positions without deeper reflection pulses in both measurement campaigns or with too poor signal quality. The THz data for specific positions is shown in (**a**) for no time difference between the deeper reflection pulses of both measurements, in (**b**) for deeper reflection pulses appearing earlier after restoration, representing a negative ToF difference, and in (**c**) for deeper reflection pulses appearing later after restoration, representing a positive ToF difference. The enlarged sections highlight these shifts of the pulse positions, which are also marked with a green circle.

reflections often occur adjacent to each other, forming spatially coherent patterns. This colour-scheme allows us to identify areas where layer changes below the surface are present, which in turn is indicative of restoration-related changes, as will be demonstrated subsequently.

The second presentation scheme is also demonstrated exemplarily for the measurement area on the knee of the sculpture of Mary. In Fig. 9d), the colormap presented displays the changes of the arrival time of the peaks (time-of-flight or ToF), which are linked to changes of the material density during the restoration process. These ToF differences reveal changes in the surface and subsurface layers of the sculpture due to restoration: A positive ToF difference (blue) indicates a higher refractive index, for example due to absorption of a consolidation material or by an additional layer, whereas a negative ToF difference (red) indicates a lower refractive index, e.g. due to the dissolution of old material or the removal of a layer. The colour bar in panel (d) ranges from red over yellow to blue and examples for each of these ToF differences are shown in panels (a–c). Positions without deeper reflection peaks in both measurements or with inadequate THz signal are represented by the colour grey. As illustrated in panels (a–c), the THz amplitude is depicted in blue against the measurement time for the data obtained prior to restoration, and in orange for the data subsequent to restoration. It shows that the deeper reflections are subject to change on an unpredictable basis due to restoration. Therefore, the positions of the largest peaks with the closest distance between the measurements prior to and following restoration are selected for the calculation of the ToF difference. These peaks are denoted by a green circle, and the magnified section on the right side of the panels highlights their position. As illustrated in panel (a), the THz data of the yellow point in panel (d) is presented as an example for a measurement point that does not exhibit a ToF difference. As illustrated in the enlarged section, the temporal position of the blue reflection pulse prior to the restoration is equivalent to the position of the orange pulse following the restoration. Panel (b) presents the THz data of the connected red point for measurement points exhibiting a negative ToF difference. As demonstrated in the expanded segment on the right of the panel, the orange reflection pulse following restoration manifests at an earlier measurement time in comparison to the blue reflection pulse prior to restoration. Finally, in panel (c), the data of the connected blue measurement point is shown as an example for positions with positive ToF difference. As illustrated in the expanded segment on the right side of the panel, the blue reflection peak from before the restoration appears, reversed to panel (b), at an earlier measurement time than the orange reflection peak after the restoration. As previously mentioned, in panel (d), material changes can be readily identified by examining the sections exhibiting higher ToF variations in proximity to the regions demonstrating lower ToF differences.

The presentation schemes shown in Figs. 8 and 9 both are based on the underlying THz data. A comparison of the two figures reveals that the coloured data points from both presentation schemes do not overlap, as they are contingent on mutually exclusive conditions in relation to the THz measurement data. Consequently, both presentation schemes are required to facilitate the interpretation of subsurface changes resulting from restoration in a substantial portion of the measurement area. Thus, we conclude that a single presentation scheme provides a limited understanding of the subject matter and does not offer a comprehensive overview.

Connection between THz data and restoration measures

The following figures examine the connection between both presentation schemes of the THz data and the restoration measures that were performed at the respective measurement areas.

Figure 10 shows the THz data and therein observable restoration changes for the measurement area at the knee of the sculpture of Mary. The figure contains four panels, which consist of the image of the sculpture with the bordered measuring area (a) along with a larger photograph of the knee in panel (b) with the measurement area digitally marked in a transparent green. In addition, the presentation schemes discussed above are shown again in panels (c and d), respectively. There are several encircled areas that highlight where the THz data reflect changes introduced by restoration and where this corresponding location is in the photography in panel (b). Panel (c) shows the first presentation scheme, which describes the creation and vanishing of subsurface layers from the appearance or disappearance of deeper THz reflection pulses. The detection of these layers can be influenced by the moisture content of the sculpture, but their position and relative proximity to the surface make this much less likely than changes made and materials used during the restoration process. The red ellipse in this panel marks several red points close to a crevice. This indicates the bonding of layers close to the crack due to restoration. Below this ellipse is a black circle with an arrow inside. It marks a relatively large area of connected blue points

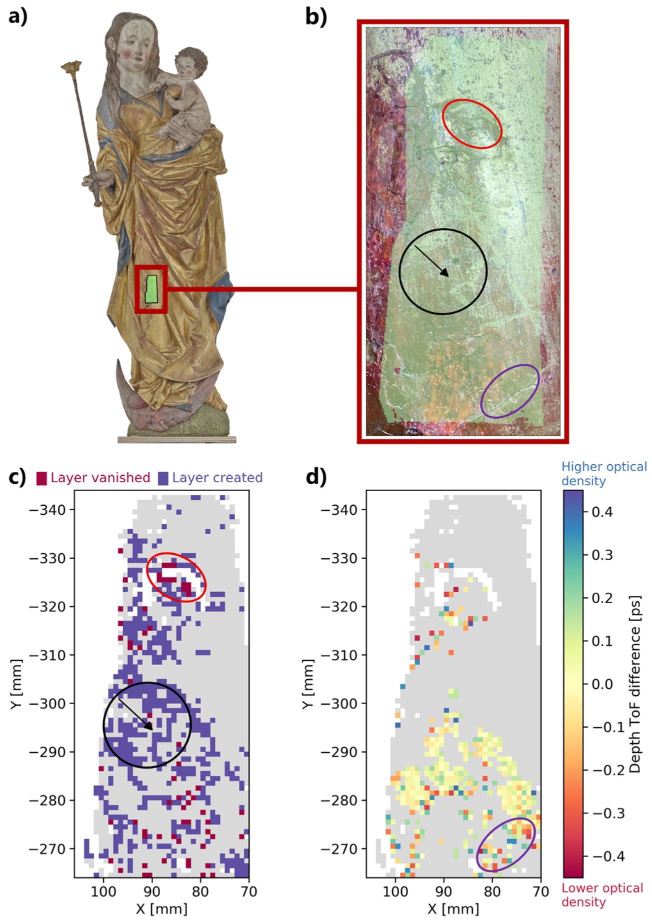

Fig. 10 | Results for the area on the knee of the sculpture of Mary with marked areas of interest for restoration changes. In the upper row, (**a**) shows an image of the sculpture with the measured area marked in green and (**b**) a closeup of the measured area. (**c**) Presents the THz data plotted following the “first THz presentation scheme”, which visualises the creation and vanishing of subsurface layers, while (**d**) presents the THz data plotted following the “second THz presentation scheme”, which visualises shifts of subsurface reflections caused by changes in optical density. Changes owing to the restoration are observable in the marked areas: The red ellipse indicates bonding of layers close to the crevice, the black circle with arrow indicates new layers in flow direction of a consolidation material introduced in the crack at the edge. The purple ellipse indicates refractive index changes through kitting and retouching.

that show the creation of new subsurface layers in the flow direction of a consolidation material injected into a crack near the origin of the arrow.

In panel (d) the second presentation scheme is shown, which describes changes in optical and therefore material density from the time shift of deeper THz reflection pulses due to restoration. In this instance, the presence of a purple ellipse at the lowermost edge of the measurement area denotes a region characterised by a more pronounced time of flight difference divergence. This demonstrates alterations in comparison to the remaining region, manifesting as a more pronounced shift in the refractive index and the optical density. This is due to the processes of kitting and retouching that occur during the restoration procedure. It can thus be posited that the retouching and filling of these areas resulted in increased material thickness. In both panels (c and d) one notices a relatively large grey section in the upper right quarter of the measurement area. The reason for this becomes obvious from the photograph in panel (b), where one can see that this area is strongly poliment gilded and therefore opaque for the THz radiation. One can notice that most observable changes in the THz data are close to cracks and crevices of the sculpture. This illustrates very well that the most extensive restorations were indeed carried out in these regions.

The results for the hip area of the infant Jesus figure are shown in Fig. 11. A comparison of the photos and the THz measurement data clearly reveals changes due to restoration. This figure comprises four panels, with panel (a) displaying the position of this hip section which has been measured. The second panel (b) presents a close up of the measured area indicated by a transparent green. Panels (c and d), respectively show the THz data plotted following the two presentation schemes. Several sections of the area show pronounced changes in the THz data, which could potentially correlate with alterations introduced during the restoration process. These sections are marked in the THz results, alongside the corresponding positions in the photography. The initial segment that calls for attention in panel (c) is a black triangle accompanied by an arrow, which delineates a connected segment of blue points. These points indicate the formation of new subsurface layers in one of the assumed flow directions of a consolidation material. This material was injected into the crack at the upper corner of the triangle, as indicated by the arrow denoting the possible flow direction. As illustrated below, the triangle is accompanied by a series of red points, marked by a red ellipse. The points in question illustrate the binding of subsurface layers due to restoration in close proximity to the encircled crevice in panel (b). As illustrated in panel (d), the purple ellipse situated in the upper right of the measurement area encircles a larger area of points with a reduced density. This can be attributed to the removal of surface contamination during cleaning in the preservation process. The turquoise rectangle positioned slightly lower on the left encircles multiple blue points of enhanced optical density, a phenomenon that we primarily attribute to the incorporation of a consolidation material, which has led to an augmentation of the refractive index within this particular region.

Overall, the data comparison before and after the conservation treatment reveals alterations in several sections of both measurement areas related to various changes in THz reflection pulses. These changes can be attributed to different conservation measures applied to the structure on and below the surface of the sculpture. The comparison of the data presented here suggests that the use of consolidation materials leads to the formation of reflective substrate layers or to an increase in the refractive index and density of the wood or lacquer layer. In addition, the adhesion of loose layers and the influence of surface cleaning can be observed.

Discussion

This article demonstrates that the restoration process that we performed on a wooden sculpture produced measurable changes of the reflected THz signals from this structure. In order to reach this conclusion, a comparative analysis of the results of two THz measurement campaigns was conducted. These campaigns were conducted in two distinct temporal periods: the first prior to the restoration of the wooden sculpture from the choir room of the Isenhagen monastery, and the second following the completion of the restoration. It is important to note that this comparison requires prior knowledge of the materials being examined. For this purpose, a database was created containing measurements of the wood in question and the conservation materials used.

As shown in the THz diagrams, several areas within the measurement surfaces were identified that were affected by different aspects of the conservation process. These included surface cleaning, visible through the refractive index change at the upper right of the hip measurement area, the percolation of consolidation materials beneath the surface, evident through the creation of new subsurface reflection peaks below defects used for injection in both areas, and the adhesion of loose paint layers and wood structures near cracks, apparent through the vanishing of subsurface reflection peaks close to crevices in both examined areas. In other words, from changes in the THz reflection data, we were able to identify and relate them to subsurface changes introduced by the restoration process. However, independent verification of the observed changes was not possible as this would require destructive approaches such as dissecting the sculpture we try to preserve.

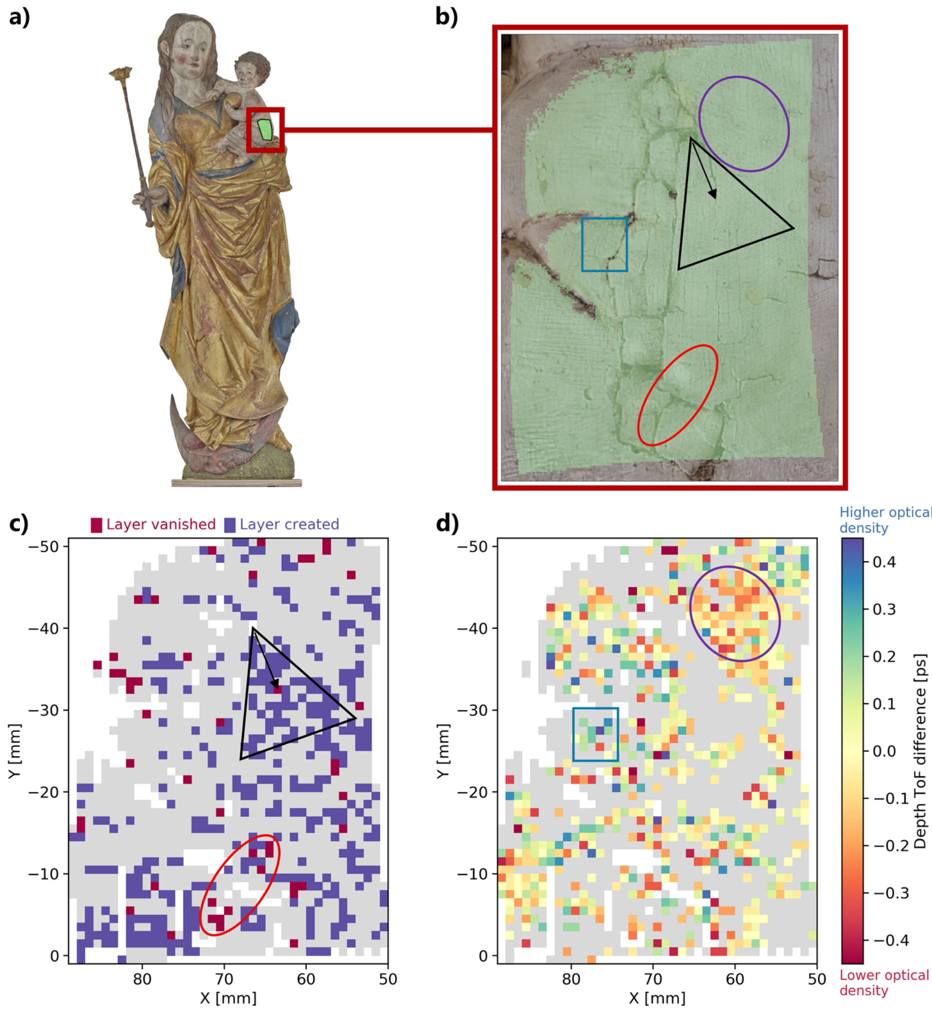

Fig. 11 | Results for the area at the hip of infant Jesus in the arm of the sculpture of Mary with marked areas of interest for restoration changes. (**a**) Shows an image of the sculpture with the measured area marked in green and (**b**) a closeup of the measured area. (**c**) Presents the THz data plotted following the "first THz presentation scheme", which visualises the creation and vanishing of subsurface layers, while (**d**) presents the THz data plotted following the "second THz presentation scheme", which visualises shifts of subsurface reflections caused by changes in optical density. Changes from restoration are observable in the marked areas: The black triangle with an arrow shows new layers created in flow direction of a consolidation material introduced in the crack at the triangle tip. The red ellipse indicates the bonding of layers near to the crevice. The purple ellipse indicates the reduction of optical density due to the removal of surface contamination. The turquoise rectangle indicates an increase in optical density due to the introduction of consolidation material.

The integration of THz measurements into conservation procedures has the potential to support conservators, even when all factors influencing measurement deviations are included in the evaluation. By enabling the monitoring of selected interventions and providing an additional tool for evaluating treatment results at specific locations on an object, it can support decisions regarding the conservation of the object.

Data availability

The datasets created and/or analysed as part of this study are not publicly available due to technical constraints (large file sizes/proprietary formats), but may be requested from the corresponding author upon reasoned request.

Received: 23 March 2026; Accepted: 29 July 2026;
Published online: 08 August 2026

References

1. Abubakar, S., Liu, X. & Xiong, X. Biological deterioration and conservation of archaeological wood: a review. *North Am. Acad. Res.* **6**, 133–147 (2023).
2. Cavalli, A., Cibecchini, D., Togni, M. & Sousa, H. S. A review on the mechanical properties of aged wood and salvaged timber. *Constr. Build. Mater.* **114**, 681–687 (2016).
3. Unger, A., Schniewind, A. P. & Unger, W. Biological deterioration of wood in *Conservation of Wood Artifacts: A Handbook* 51–141 (Springer, 2001).
4. Rowell, R. M. et al. *Handbook of Wood Chemistry and Wood Composites* Second Edition (ed. Rowell, R. M.) (CRC Press, 2012).
5. Wang, Q., Feng, X. & Liu, X. Advances in historical wood consolidation and conservation materials. *BioResources* **18**, 6680–6723 (2023).
6. Linke, G. *Festigkeitssortierung von Holzbauteilen beim Bauen im Bestand: ein Beitrag zur substanzschonenden Erhaltung historischer Gebäude* PhD thesis (BTU Cottbus-Senftenberg, 2024).
7. Yu, T., Sousa, H. S. & Branco, J. M. Combination of non-destructive tests for assessing decay in existing timber elements. *Nondestruct. Test Eval.* **35**, 29–47 (2020).
8. Arakistain, I., Abascal, J. M. & Munne, O. ICT technologies for the refurbishment of wooden structure buildings. https://doi.org/10.48550/arXiv.1401.8136 (2014).
9. Osterloh, K. et al. Computed tomography with X-rays and fast neutrons for restoration of wooden artwork. *Phys. Procedia* **69**, 472–477 (2015).
10. Niemz, P. & Mannes, D. Non-destructive testing of wood and wood-based materials. *J. Cult. Herit.* **13**, S26–S34 (2012).
11. Hasenstab, A. et al. Luftultraschall und Ultraschall-Echo-Technik an Holz in *DGZfP-Berichtsband 94-CD* Plakat 54, 1–15 (DGZfP, 2005).
12. Schaible, V. Das Marienretabel von Tilman Riemenschneider in der Herrgottskirche in Creglingen - Ergebnisse einer ersten kunsttechnologischen Untersuchung. *Z Kunsttechnol. Konserv.* **32**, 5–32 (2018).
13. Buchholz, R. & Fiedler, C. Dem Chorgestühl auf die Beine helfen … – Kunstharztränkung von Holzbauteilen als letzte Chance! in Konsolidieren & Kommunizieren - Materialien und Methoden zur Konsolidierung von

Kunst- und Kulturgut im interdisziplinären Dialog (ed. Weyer, A.) 113–121 (Michael Imhof Verlag, Hildesheim/Fulda, 2018).
14. Simon, T. “Wahrlich ich sage euch; was ihr auf Erden binden werdet, soll auch im Himmel gebunden sein”: die Restaurierung des Beichtstuhles aus der Kirche zu Gross Mohrdorf. *Z. Kunsttechnol. Konserv.* **32**, 129–154 (2018).
15. Gazzola, P. et al. International charter for the conservation and restoration of monuments and sites (the Venice charter 1964). in *IInd International Congress of Architects and Technicians of Historic Monuments*, *Venice* (ICOMOS, 1964).
16. Schädler-Saub, U. Conservation ethics today: are our conservation-restoration theories and practice ready for the twenty-first century? Introductory notes to some central issues. *Protection of Cultural Heritage* **8**, 291–300 (2019).
17. Fukunaga, K. & Hosako, I. Innovative non-invasive analysis techniques for cultural heritage using terahertz technology. *Comptes Rendus. Phys.* **11**, 519–526 (2010).
18. Balzer, J. C. et al. THz systems exploiting photonics and communications technologies. *IEEE J. Microw.* **3**, 268–288 (2022).
19. Stübling, E. et al. A THz tomography system for arbitrarily shaped samples. *J. Infrared, Millim., Terahertz Waves* **38**, 1179–1182 (2017).
20. Krügener, K. et al. THz tomography for detecting damages on wood caused by insects. *Appl. Opt.* **58**, 6063–6066 (2019).
21. Stübling, E.-M. et al. Application of a robotic THz imaging system for sub-surface analysis of ancient human remains. *Sci. Rep.* **9**, 3390 (2019).
22. Manca, R. et al. Non-invasive characterization of maiolica layer structure by terahertz time-domain imaging. *Coatings* **13**, 1268 (2023).
23. Fauquet, F. et al. Terahertz frequency-modulated continuous-wave inspection of an ancient enamel plate. *Sensors* **25**, 2928 (2025).
24. Mikerov, M., Shrestha, R., van Dommelen, P., Mittleman, D. M. & Koch, M. Analysis of ancient ceramics using terahertz imaging and photogrammetry. *Opt. Express* **28**, 22255–22263 (2020).
25. Zhai, M., Locquet, A., Shi, H., Monfort, C. C. & Citrin, D. Characterization of roman amphora sherds using terahertz time-of-flight tomography. in *Proc. 2023 IMEKO TC-4 International Conference on Metrology for Archaeology and Cultural Heritage*, *Rome, Italy* 549–553 (IEEE, 2023).
26. Meng, T. et al. Highly sensitive terahertz non-destructive testing technology for stone relics deterioration prediction using SVM-based machine learning models. *Herit. Sci.* **9**, 1–9 (2021).
27. Bandyopadhyay, A. et al. Sub-surface damage detection in marble structures using THz time domain and laser feedback interferometric imaging in *Optics for Arts*. *Archit. Archaeol. VIII* **11784**, 119–127 (2021).
28. Lambert, F. E. et al. Layer separation mapping and consolidation evaluation of a fifteenth century panel painting using terahertz time-domain imaging. *Sci. Rep.* **12**, 21038 (2022).
29. Reyes-Reyes, E. S. et al. Terahertz time-domain imaging for the examination of gilded wooden artifacts. *Sci. Rep.* **14**, 6261 (2024).
30. Artesani, A. et al. Integrated imaging and spectroscopic analysis of painted fresco surfaces using terahertz time-domain technique. *Heritage* **6**, 5202–5212 (2023).
31. Vazquez, D. A., Pilozzi, L., DelRe, E., Conti, C. & Missori, M. Terahertz imaging super-resolution for documental heritage diagnostics. *IEEE Trans. Terahertz Sci. Technol.* **14**, 455–465 (2024).
32. Dong, J., Ribeiro, A., Vacheret, A., Locquet, A. & Citrin, D. Revealing inscriptions obscured by time on an early-modern lead funerary cross using terahertz multispectral imaging. *Sci. Rep.* **12**, 3429 (2022).
33. Zhu, P., Zhang, H., Sfarra, S., Yang, D. & Maldague, X. A review of cultural heritage inspection: toward terahertz from mid-infrared region. Preprint at https://doi.org/10.48550/arXiv.2510.11521 (2025).
34. Fukunaga, K. & Picollo, M. Terahertz spectroscopy applied to the analysis of artists’ materials. *Appl. Phys. A*. **100**, 591–597 (2010).
35. Mittleman, D. M., Hunsche, S., Boivin, L. & Nuss, M. C. T-ray tomography. *Opt. Lett.* **22**, 904–906 (1997).
36. Hunsche, S., Mittleman, D. M., Koch, M. & Nuss, M. C. New dimensions in T-ray imaging. *IEICE Trans. Electron.* **81**, 269–276 (1998).
37. Koch, M., Mittleman, D. M., Ornik, J. & Castro-Camus, E. Terahertz time-domain spectroscopy. *Nat. Rev. Methods Prim.* **3**, 48 (2023).
38. Smith, P. R., Auston, D. H. & Nuss, M. C. Subpicosecond photoconducting dipole antennas. *IEEE J. Quantum Electron.* **24**, 255–260 (1988).
39. Grischkowsky, D., Keiding, S., Van Exter, M. & Fattinger, C. Far-infrared time-domain spectroscopy with terahertz beams of dielectrics and semiconductors. *JOSA B.* **7**, 2006–2015 (1990).
40. Walther, M., Fischer, B., Schall, M., Helm, H. & Jepsen, P. U. Far-infrared vibrational spectra of alltrans, 9-cis and 13-cis retinal measured by THz time-domain spectroscopy. *Chem. Phys. Lett.* **332**, 389–395 (2000).
41. Schmuttenmaer, C. A. Exploring dynamics in the far-infrared with terahertz spectroscopy. *Chem. Rev.* **104**, 1759–1780 (2004).
42. Vieweg, N., Shakfa, M. K., Scherger, B., Mikulics, M. & Koch, M. THz properties of nematic liquid crystals. *J. Infrared, Millim. Terahertz Waves* **31**, 1312–1320 (2010).
43. Laib, J. P. & Mittleman, D. M. Temperature-dependent terahertz spectroscopy of liquid n-alkanes. *J. Infrared Millim. Terahertz Waves* **31**, 1015–1021 (2010).
44. Jansen, C., Wietzke, S., Astley, V., Mittleman, D. M. & Koch, M. Mechanically flexible polymeric compound one-dimensional photonic crystals for terahertz frequencies. *Appl. Phys. Lett.* **96**, 111108 (2010).
45. Lloyd-Hughes, J. & Jeon, T.-I. A review of the terahertz conductivity of bulk and nano-materials. *J. Infrared, Millim., Terahertz Waves* **33**, 871–925 (2012).
46. Taleb, F., Hernandez-Cardoso, G. G., Castro-Camus, E. & Koch, M. Transmission, reflection, and scattering characterization of building materials for indoor THz communications. *IEEE Trans. Terahertz Sci. Technol.* **13**, 421–430 (2023).
47. Hu, B. B. & Nuss, M. C. Imaging with terahertz waves. *Opt. Lett.* **20**, 1716–1718 (1995).
48. Zeitler, J. A. et al. Analysis of coating structures and interfaces in solid oral dosage forms by three dimensional terahertz pulsed imaging. *J. Pharm. Sci.* **96**, 330–340 (2007).
49. Jansen, C. et al. Terahertz imaging: applications and perspectives. *Appl. Opt.* **49**, E48–E57 (2010).
50. Guerboukha, H., Nallappan, K. & Skorobogatiy, M. Toward real-time terahertz imaging. *Adv. Opt. Photonics* **10**, 843–938 (2018).
51. Wilk, R. et al. THz time-domain spectrometer based on LT-InGaAs photoconductive antennas exited by a 1.55 μm fibre laser. in *Proc. Conference on Lasers and Electro-Optics/Quantum Electronics and Laser Science Conference and Photonic Applications Systems Technologies* (Optica Publishing Group, 2007).
52. Vieweg, N. et al. Terahertz-time domain spectrometer with 90 dB peak dynamic range. *J. Infrared, Millim. Terahertz Waves* **35**, 823–832 (2014).
53. Dohms, A. et al. Fiber-coupled THz TDS system with mW-level THz power and up to 137-dB dynamic range. *IEEE Trans. Terahertz Sci. Technol.* **14**, 857–864 (2024).
54. Selesnick, I. Sparse deconvolution (an MM algorithm). *Connexions* https://eeweb.engineering.nyu.edu/iselesni/lecture_notes/sparse_deconv/SparseDeconv.pdf (2012).
55. Dong, J., Wu, X., Locquet, A. & Citrin, D. S. Terahertz superresolution stratigraphic characterization of multilayered structures using sparse deconvolution. *IEEE Trans. Terahertz Sci. Technol.* **7**, 260–267 (2017).
56. Selesnick, I. Penalty and shrinkage functions for sparse signal processing. *Connexions* **11**, https://eeweb.engineering.nyu.edu/iselesni/lecture_notes/sparse_penalties/sparse_penalties.pdf (2012).

Acknowledgements

The authors would like to thank the Klosterkammer Hannover for the provision of the object of study, and the Niedersächsisches Landesamt für

Denkmalpflege Hannover for professional consultation. The authors would like to express their gratitude to the Deutsche Bundesstiftung Umwelt (Germany) for financial support.

Author contributions

C.M. and K.K. wrote the main manuscript, with the exception of the chapter on restoration, which was written by R.J. Furthermore, R.J. was tasked with the responsibility of undertaking the conservation work necessary for the measurements of the statue of the sculpture of Mary. A.J. has programmed the multimatrix Sparse deconvolution algorithm for data analysis. J.O. and J.T. assisted with the two on-site measurement campaigns. E.C.C. processed the data for Fig. 2 and prepared the presentation; he also processed part of Fig. 1. M.K., W.V. and R.P. provided expert advice on the analysis. All authors have read and approved the manuscript.

Funding

Open Access funding enabled and organized by Projekt DEAL.

Competing interests

The authors declare no competing interests.

Additional information

Correspondence and requests for materials should be addressed to Kirsti Krügener.